LANGMUIR

pubs.acs.org/Langmuir Article

Conversion of Polymer Surfaces into Nonwetting Substrates for Liquid Metal Applications

Sachin Babu, Behnoush Dousti, Gil Sik Lee, and Jeong-Bong Lee*

Cite This: *Langmuir* 2021, 37, 8139–8147 Read Online

ACCESS | Metrics & More | Article Recommendations | Supporting Information

ABSTRACT: Liquid metal-based applications are limited by the wetting nature of polymers toward surface-oxidized gallium-based liquid metals. This work demonstrates that a 120 s CF_4/O_2 plasma treatment of polymer surfaces—such as poly(dimethylsiloxane) (PDMS), SU8, S1813, and polyimide—converts these previously wetting surfaces to nonwetting surfaces for gallium-based liquid metals. Static and advancing contact angles of all plasma-treated surfaces are >150°, and receding contact angles are >140°, with contact angle hysteresis in the range of 8.2−10.7°, collectively indicating lyophobic behavior. This lyophobic behavior is attributed to the plasma simultaneously fluorinating the surface while creating sub-micron scale roughness. X-ray photoelectron spectroscopy (XPS) results show a large presence of fluorine at the surface, indicating fluorination of surface methyl groups, while atomic force microscopy (AFM) results show that plasma-treated surfaces have an order of magnitude greater surface roughness than pristine surfaces, indicating a Cassie−Baxter state, which suggests that surface roughness is the primary cause of the nonwetting property, with surface chemistry making a smaller contribution. Solid surface free energy values for all plasma-treated surfaces were found to be generally lower than the pristine surfaces, indicating that this process can be used to make similar classes of polymers nonwetting to gallium-based liquid metals.

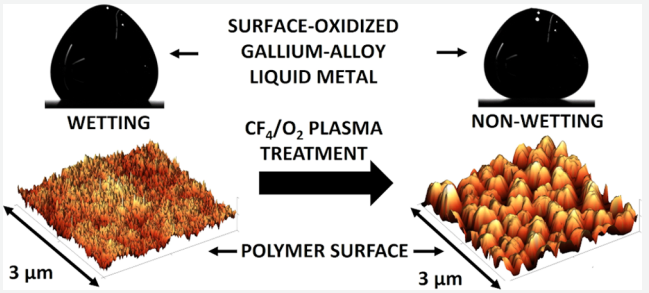

INTRODUCTION

Eutectic alloys such as eGaIn (75% Ga, 25% In) and galinstan (68.5% Ga, 21.5% In, 10% Sn) have been receiving growing attention in a variety of applications due to their relatively high electrical and thermal conductivity, nontoxicity, and low vapor pressure when compared with other room-temperature liquid metals, such as mercury.[1] Compared with solid conductive substrates, such as copper, liquid metals allow the fabrication of conductive structures, at milli,[2] micron,[3] and sub-micron[4] scales, that can be flexible, stretchable, and deformable while retaining its conductivity. Recent research shows that gallium-based liquid metals have been used to develop soft flexible and stretchable electronics,[5,6] radio-frequency (RF) antennas,[7−11] switches,[12−16] rotating liquid drops,[17,18] frequency selective surfaces,[19−22] three-dimensional (3D)-printed structures,[23−28] and composites.[29−31]

A common feature of these liquid metal devices listed above is that the liquid metal is not mobile in air. Instead, the liquid metal slug is either embedded within the entire volume of the channel or encapsulated in an insulating liquid, with the insulating liquid typically filling the entire volume of the channel.[20] The reason for this is because gallium-based liquid metals are wetting to a variety of materials, and once it fills a channel, it is quite difficult to remove.[32] The cause of this wetting property comes from the liquid metal's nature to spontaneously oxidize in ambient air, forming a few nanometers of a thin oxide shell consisting of Ga_2O and Ga_2O_3,[33] and it is this oxide shell that has the property of being strongly adhesive to a variety of materials.[32,34] This wetting property applies to a wide variety of surfaces and likely has hindered progress in applications that require the liquid metal to be nonwetting, such as droplet microfluidics, soft matter computing for soft robotics,[35] or triboelectric nanogenerators (TENGs).[36] Thus, developing a quick process that can be applied to a variety of surfaces to make these permanently ubiquitously nonwetting to gallium-based liquid metals should help promote the development of applications that take advantage of the nonwetting property.

Several methods have been developed to counter the wetting nature of surface-oxidized gallium-based liquid metals (oxLMs). One method involves removing the oxide layer using caustic agents, such as hydrochloric acid (HCl).[37,38] While this method is highly effective, allowing electrochemical actuation methods,[39,40] using such caustic agents will restrict material options, impose extra safety measures, and, due to its reactive and evaporative properties, will need to be replenished

Received: March 11, 2021
Revised: June 10, 2021
Published: June 28, 2021

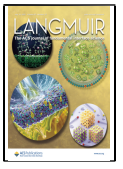

https://doi.org/10.1021/acs.langmuir.1c00689
Langmuir 2021, 37, 8139−8147

over time. Another method involves introducing foreign thin films such as Neverwet,[41] gallium thin films,[42] or fumed silica nanoparticles[43] as a coating on elastomeric substrates. Neverwet is suitable for milli-scale patterns, having a reported lowest thickness limit of about 750 μm,[41] which limits the feature size of microstructures; additionally, experience has shown that the coating tends to peel from substrates over time. The method of gallium thin-film coating allows for ubiquitous nonwetting surfaces; however, the coating is opaque and conductive. This conductive layer may not be compatible with certain electronic and RF applications that require a non-conductive substrate. The method for fumed silica nanoparticle coating requires an organic solvent to create a dispersed mixture which can be applied to a surface or injected into a closed microfluidic channel. However, the authors report that the method does not work well on heavily cross-linked polymers (such as SU8) or polymers that have a low glass transition temperature.[43] Multistep fabrication of hierarchical micro/nanoscale structures is another method that has been shown to create nonwetting surfaces with high contact angles (CA) after a C_4F_8 Teflon-like coating is applied on pillar arrays.[44] However, there is no clear way to apply a similar fabrication method to create such structures on sidewalls for microchannels.[45]

Two methods have been reported on making a nonwetting surface for oxLMs through the creation of sub-micron scale roughness of the polymer surface. The first method involves the casting of poly(dimethylsiloxane) (PDMS) in black silicon,[46] and the second involves exposure of PDMS surface to sulfuric acid.[47] The method of casting PDMS in black silicon to create sub-micron surface roughness is promising; however, the process is significantly long (several hours) with no study on whether it can be applied to sidewall features.[46] The method of sulfuric acid exposure by Li et al. can be used to create sub-micron surface roughness by injecting the acid into premade PDMS microfluidic channels and flushing it out with water followed by drying.[47] However, it is unclear if the method would create similar nonwetting surface roughness for other polymer classes; additionally, this method would require high pumping pressures to inject the liquid into smaller microscale channels, which would risk delamination or bursting of the microfluidic device.

This work shows that exposure to a 3:1 CF_4/O_2 plasma treatment for 120 s converts polymeric surfaces into visibly smooth, permanent intrinsically nonwetting surfaces for surface-oxidized gallium-based liquid metals. In contrast with other methods, this single-step process utilizes no caustic agents or coatings and can be used on a variety of polymers. Four standard polymers, before and after plasma treatment, are studied by conducting contact angle goniometry along with chemical and physical surface characterizations to determine the underlying cause of the nonwetting property.

EXPERIMENTAL SECTION

Materials and Fabrication. The four polymer materials prepared for plasma treatment are SYLGARD 184 PDMS (Dow Chemical Company, Midland, MI), MicroChem SU8-2010 (Kayaku Advanced Materials, Inc., Westborough, MA), MicroChem S1813, and Kapton tape (3 mils, adhesive on one side) (DuPont, Wilmington, DE). Each material was chosen as a representative of a class of polymers for which the plasma treatment could produce similar nonwetting property. PDMS represents the class of silicone polymers, SU8-2010 represents the class of negative photosensitive resists, S1813 represents the class of positive photosensitive resists, and Kapton tape represents polyimides.

To create pristine samples, each liquid polymer was spun on a bare 3″ <100> silicon wafer at 3000 rpm for 75 s. The PDMS polymer was prepared by mixing the prepolymer and polymerizing agent from the silicone elastomer kit using the standard 10:1 ratio by weight of prepolymer to polymerizing agent, which was degassed in a vacuum chamber for 1 h; the mixture was used within 10 min after vacuum desiccation. The other liquid polymers (SU8, S1813) required no prior preparation. After spinning, the PDMS on wafer was baked in a 95 °C oven for 10 min. The SU8-2010 on wafer was baked on a 115 °C hotplate for 1 min and subsequently exposed to i-line (365 nm) UV light (900 W) for 2 min to ensure crosslinking. The S1813 on wafer was baked on a 115 °C hotplate for 1 min. S1813 was left unexposed. Sections of the polyimide tape were cut and affixed onto a bare silicon wafer.

Half of the pristine samples were treated to 120 s of a 3:1 ratio CF_4/O_2 plasma (250 W, 100 mTorr, 3 sccm O_2, 9 sccm CF_4) using a Trion Sirius-T2 RIE Etcher (Trion Technology, Tempe, AZ) to create plasma-treated samples. Enough pristine and plasma-treated samples were created to allow for a single measurement of a sample surface. No sample subjected to a measurement was reused.

Contact Angle Measurements. The Drop Shape Analysis System DSA30B (KRÜSS GmbH, Hamburg, Germany) was used to make contact angle measurements using their DSA4 image analysis software. The liquid metal used is galinstan (Ga 68.5%, In 21.5%, Sn 10%) (Changsha Rich Nonferrous Metals Co., Ltd., Hunan, China). The liquid metal was loaded into a SY3601 syringe (4.706 mm diameter, 1.0 mL, Henke Sass Wolf GmbH, Tuttlingen, Germany) with a KRÜSS NE47 needle (0.7 mm OD, 38 mm long, blunt polypropylene needle). Static and dynamic contact angles of each surface were characterized by dropping ~8 μL liquid metal droplets, naturally oxidized in ambient air, onto each surface, which lay on the horizontally leveled stage of the DSA30B system. The capillary length ($k^{-1} = \sqrt{\gamma/\rho g}$) for liquid metal is 2.8 mm (galinstan surface tension, γ, and density, ρ, of 510 mN/m and 6440 kg/m^3, respectively, from Liu et al.,[1] with g = 9.8 m/s^2), which requires liquid metal droplets to have a radius less than 2.8 mm to avoid the effects of gravity. An 8 μL drop has roughly a 0.9 mm radius, which meets the requirement. Picture or video recordings were made of each droplet, and the DSA4 software's image processing algorithm was used to automatically detect the left and right contact angles and take an average; this average is treated as the contact angle measurement.

Apparent surface free energy measurements of both the pristine and plasma-treated polymer surfaces were determined from static contact angle (SCA) measurements using two standard liquids, deionized water (DIW) (Item #R-950-1, CAS #7732-18-5, PTI Process Chemicals, Ringwood, IL) and diiodomethane (DIO) (CAS #75-11-6, Sigma, Saint Louis, MO). The static contact angles for 4 μL of deionized water droplets for 4 μL of diiodomethane droplets on the polymer surfaces were measured using the ramé-hart manual goniometer (Model #50-00-115, ramé-hart, Mountain Lakes, NJ). The capillary length is 2.7 for deionized water and 2.3 for diiodomethane. A 4 μL drop has roughly a 0.7 radius, which meets the requirement for avoiding the effects of gravity when measuring contact angles.

Contact angle (CA) measurements were performed on all four materials, for both pristine and plasma-treated samples, by recording a set of five independent measurements for static, advancing, and receding contact angles (RCAs). The average and standard deviation of these five measurements were used to estimate the mean contact angle value and the error on it, respectively. No sample surfaces were reused after a single-contact measurement. Only center sections of Si wafers (away from edges), which have the most uniform thickness and uniform plasma exposure, were used. These protocols were followed to ensure that each data point represented the same experimental setup as much as possible.

Although contact angle measurements can be used to estimate the work spent to create new interfaces, for example, as described by the

https://doi.org/10.1021/acs.langmuir.1c00689
Langmuir 2021, 37, 8139−8147

works of Makkonen et al.,[48] there seems to be a debate on whether these can be used to determine work of adhesion.[34,49] Furthermore, for the special case of liquid metals, the viscoelastic and adhesive nature of the oxide skin may affect the behavior of the advancing and receding contact lines to act otherwise than what would be expected from a true liquid. Thus, measuring the work of adhesion using contact angles may not produce expected results for surface-oxidized liquid metals. However, there have been recent reports of new measurement techniques that rely on the separation of the liquid droplet from the solid surface, such as the centrifugal adhesion balance,[34,50] or the speaker cone system,[51] and these may prove to be more useful methods for accurately measuring the work of adhesion of surface-oxidized liquid metals than contact angle measurements.

Surface Characterization. Chemical characterization of the surface was done using X-ray photoelectron spectroscopy (XPS), which uses the photoelectric effect to identify elements that exist at the surface of a material. The characterization was performed using the PHI VersaProbe II XPS system (Chigasaki, Japan) that has a monochromatic aluminum K Alpha X-ray radiation source (1486.6 eV, 50.2 W) with beam diameter 200 μm at 45° angle in FAT mode. The pass energy for survey spectra was 187.85 eV, while the pass energy for high-resolution spectra was 23.50 eV. Since the sample surfaces are nonconducting polymers, automated neutralization was used (2 V, 22.0 μA). MultiPak v9 software was used to perform the peak shift-correction on a sample's spectrum to the reference C 1s binding energy (BE) of 284.8 eV; the software was also used for deconvolution analysis of high-resolution C 1s peaks. Physical characterization was performed using atomic force microscopy (AFM) by the Jupiter XF Atomic Force Microscope system (Asylum Research, Santa Barbara, CA), with an AC160-TS cantilever tip, in tapping mode. A 5 μm × 5 μm section was scanned to create images with 256 × 256 pixels for plasma-treated materials, which has submicron features, and images with 512 × 512 pixels for pristine materials, which has nanometer features. From each 5 μm × 5 μm section, an artifact-free 3 μm × 3 μm region was selected.

RESULTS AND DISCUSSION

Contact Angle Measurements. Static contact angle (SCA) results of 8 μL of sessile surface-oxidized galinstan droplets are shown in Figure 1. For pristine materials, the CAs range from 123.9 ± 4.5 to 130.1 ± 3.0°, a total range of 13.7° (Figure 1, bottom). The wide range of angles indicates the different surface chemistry of each material in determining a contact angle. The high contact angles (>90°, typically considered lyophobic) are due to the high surface tension of the liquid metal encased in the oxide skin. For plasma-treated materials, the CAs range from 154.1 ± 1.0 to 156.7 ± 0.5°, a range of 4.0° (Figure 1, top), demonstrating that all of the surfaces are superlyophobic to oxLM.

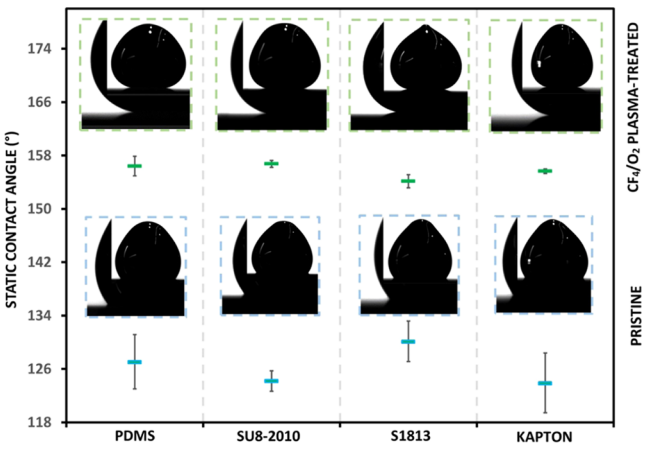

Figure 1. Static contact angle measurements of plasma-treated (top) and pristine (bottom) polymer films on a silicon wafer using surface-oxidized galinstan droplets. Eight microliters of liquid metal droplets were used; all droplet radii are ∼2 mm. Each data point has an associated inset figure that shows a close up of the left contact angle of the liquid metal droplet taken from the DSA4 goniometer camera, and a further inset showing the whole droplet to show the vertical axis symmetry, droplet shape, and visually observable difference in contact angles.

Dynamic contact angle results are shown in Figure 2. Each measurement had the needle 2 mm from the surface, infusing 5−8 μL of Galinstan to form an advancing contact angle (ACA) line, and withdrawing an excess of 8−15 μL to form a receding contact angle to break contact with the surface to test for the nonwetting property. For pristine samples (Figure 2a), advancing contact angles (ACAs) range from 140.8 ± 2.0 to 150.6 ± 0.7°, a total range of 12.5°; the receding contact angles (RCAs) range from 17.7 ± 0.5 to 24.0 ± 2.1°, a total range of 8.9°; the contact angle hysteresis (CAH) ranges from 121.5 to 130.8°, which indicates a highly wetting surface, as demonstrated by the liquid metal residue left on the surface (Figure 2a, "wetting" inset). For plasma-treated samples (Figure 2b), advancing contact angles (ACAs) range from 152.2 ± 0.9 to 154.7 ± 0.4°, a total range of 3.8°; receding contact angles (RCAs) range from 141.4 ± 1.9 to 147.6 ± 2.4°, a total range of 10.5°; the contact angle hysteresis (CAH) ranges from 6.4 to 10.7°, which indicates a highly nonwetting surface, as indicated by the lack of liquid metal residue on the surface (Figure 2b, "nonwetting" inset).

Surface Chemistry. XPS measurements were conducted on all samples to determine the changes in surface chemistry that results from CF_4/O_2 plasma treatment. Figure 3a,b, shows the survey for PDMS and SU8, respectively; XPS surveys for S1813 and Kapton are provided in Figure S1 in the Supporting Information section and show similar results. For all surveys, the C 1s, O 1s, F 1s, peaks, if present, are identified; the O KLL and F KLL Auger lines are also identified for clarity. Si 2s and Si 2p peaks are identified for the silicone polymer.

In the pristine PDMS survey, labeled "PDMS-PR" in Figure 3a, the C 1s peak corresponds to C−H and C−Si bonds (284.8 eV); there are no C−C bonds in PDMS. The key feature to observe in the survey is the lack of fluorine (F 1s and F KLL) peaks. The plasma-treated PDMS survey, labeled "PDMS-PL" in Figure 3a, has the fluorine F 1s and F KLL peaks, indicative of fluorination of methyl groups in PDMS.

The fluorination of methyl groups in PDMS has been reported by Manca et al.,[52] which studied the effect of CF_4 plasma on the chemistry and topology of PDMS. Comparing the C 1s XPS spectrum of PDMS-PR (Figure 4a) to the C 1s spectra of PDMS-PL (Figure 4c), it is very likely that the CF_4:O_2 plasma causes different degrees of fluorination (CH_3 to CFH_2, CH_3 to CF_2H, and CH_3 to CF_3) of the surface methyl groups of PDMS. For Figure 4c, the deconvolution of peaks indicates that about 20% of the PDMS surface methyl groups has some degree of fluorination, most of it likely CFH_2 (blue curve) and CF_2H (green curve).

Figures 3b and 4b show that the survey spectra for pristine SU8 (labeled "SU8-PR") already have the fluorine F 1s and F KLL peaks. This is due to the triarylsulfonium hexafluoroantimonate component in SU8, which is the UV-sensitive crosslinking initiator mixed in with the SU8 epoxy resin, and a significant amount remains even after UV exposure.[53] Plasma treatment of SU8 ("SU8-PL") introduces fluorination of the

https://doi.org/10.1021/acs.langmuir.1c00689
Langmuir 2021, 37, 8139−8147

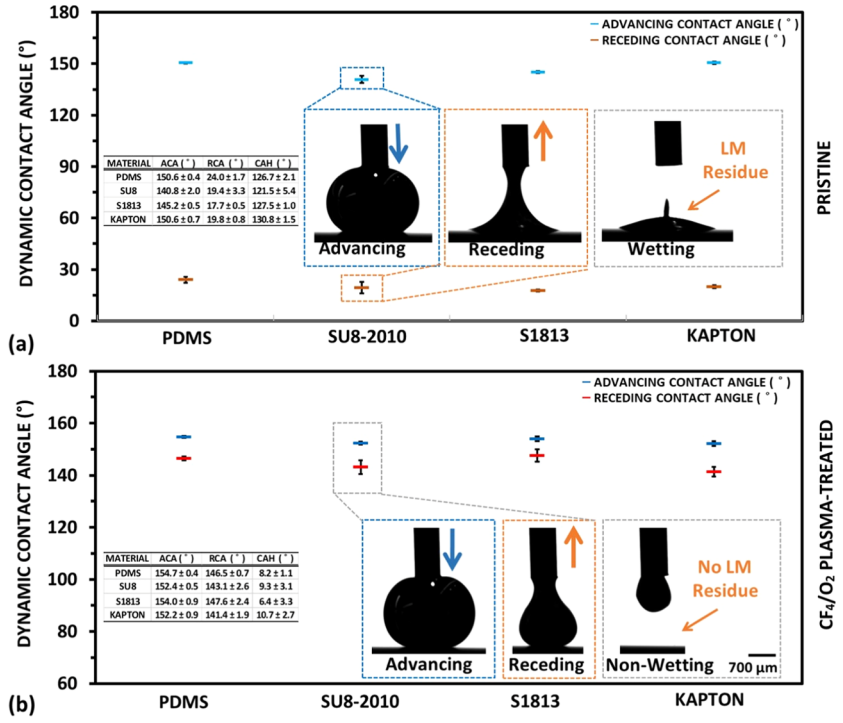

Figure 2. Dynamic contact angle for (a) pristine and (b) plasma-treated materials. The blue arrow indicates infusion, the orange arrow indicates withdrawal, and LM stands for "liquid metal".

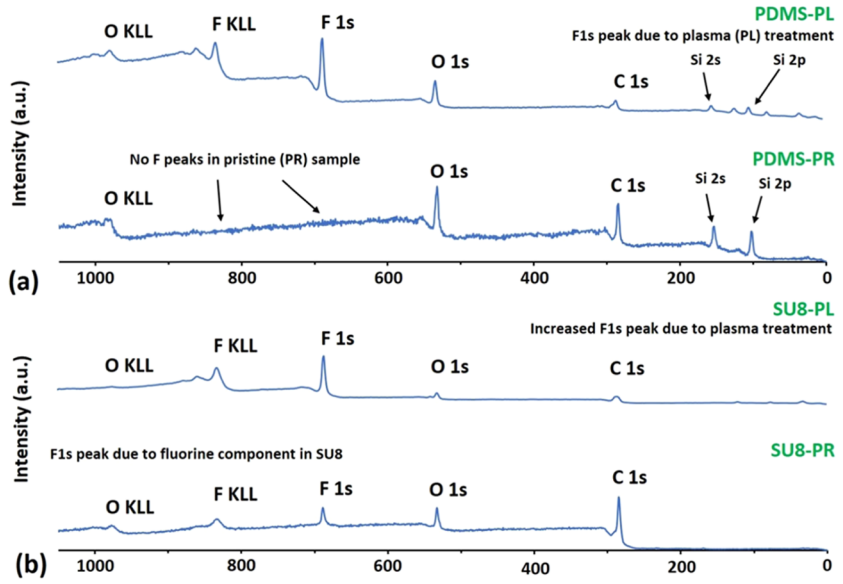

Figure 3. XPS survey of (a) plasma-treated (PDMS-PL curve) and pristine (PDMS-PR curve) PDMS; (b) plasma-treated (SU8-PL curve) and pristine (SU8-PR curve) SU8-2010.

large number of methylated carbons in SU8. This can be seen in the larger intensity of the F 1s peak when compared with the C 1s peak (Figure 3b, SU8-PL survey), and in observing that the C 1s XPS spectra of SU8-PL (Figure 4d) show that the C−F peak has near equal intensity to the C−C peak.

These results indicate that the plasma treatment is a chemical modification of the surface which alters the surface energy, and that the amount of modification is unique to each material. Manca et al.[52] clearly demonstrated that a pure CF_4 plasma does indeed lower surface energy of PDMS through chemical modification of methyl groups by fluorination, and each material has a unique number of methyl groups leading to different amounts of fluorination. However, plasma treatment also creates surface roughness, which reduces the role of chemical modification by reducing the contact area of the droplet and the material surface. This is especially the case if the surface roughness produces a Cassie−Baxter wetting interface against liquid metals.

Surface Roughness Investigation Using AFM. AFM measurements can be used to determine the differences in surface roughness between pristine and plasma-treated materials. Figure 5 visually shows the significant increase in

https://doi.org/10.1021/acs.langmuir.1c00689
Langmuir 2021, 37, 8139−8147

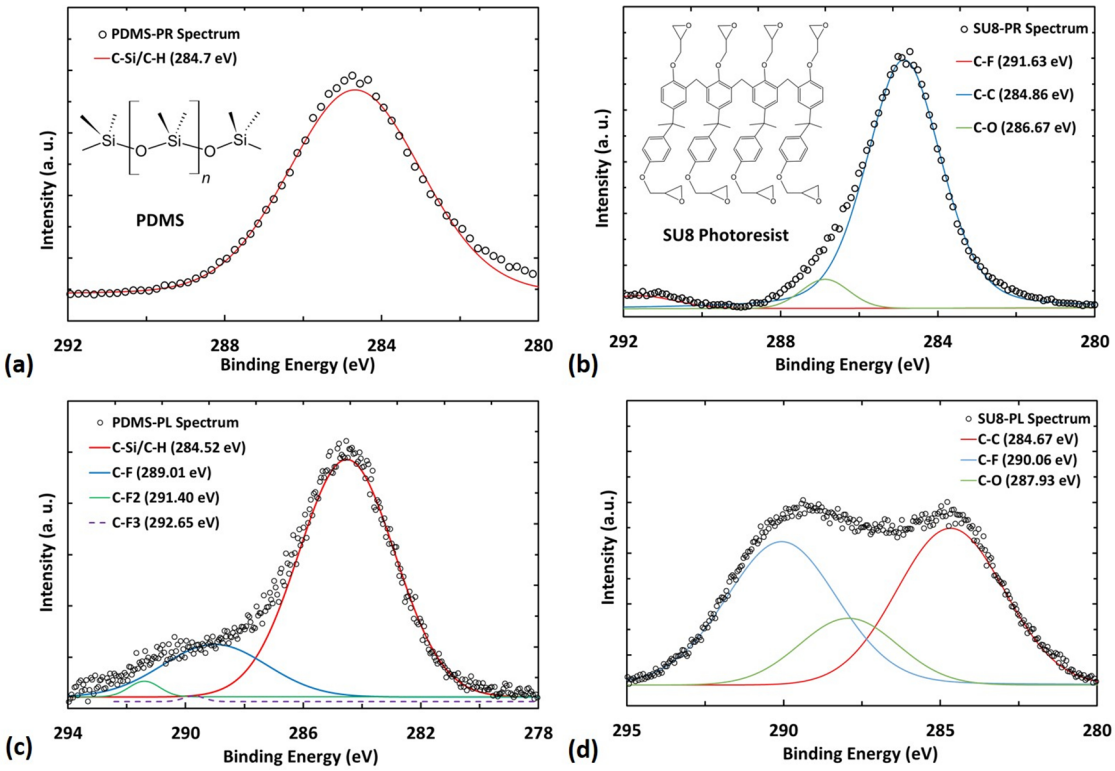

Figure 4. C 1s XPS spectra for (a) pristine PDMS (PDMS-PR), the inset is the molecular structure of PDMS (redrawn from Seethapathy et al.[54]); (b) pristine SU8 (SU8-PR), the inset is the molecular structure of SU8 (redrawn from del Campo et al.[55]); (c) plasma-treated PDMS (PDMS-PL); and (d) plasma-treated SU8 (SU8-PL). The binding energies were obtained from Bratt, et al.[56] and Cordeiro et al.[57]

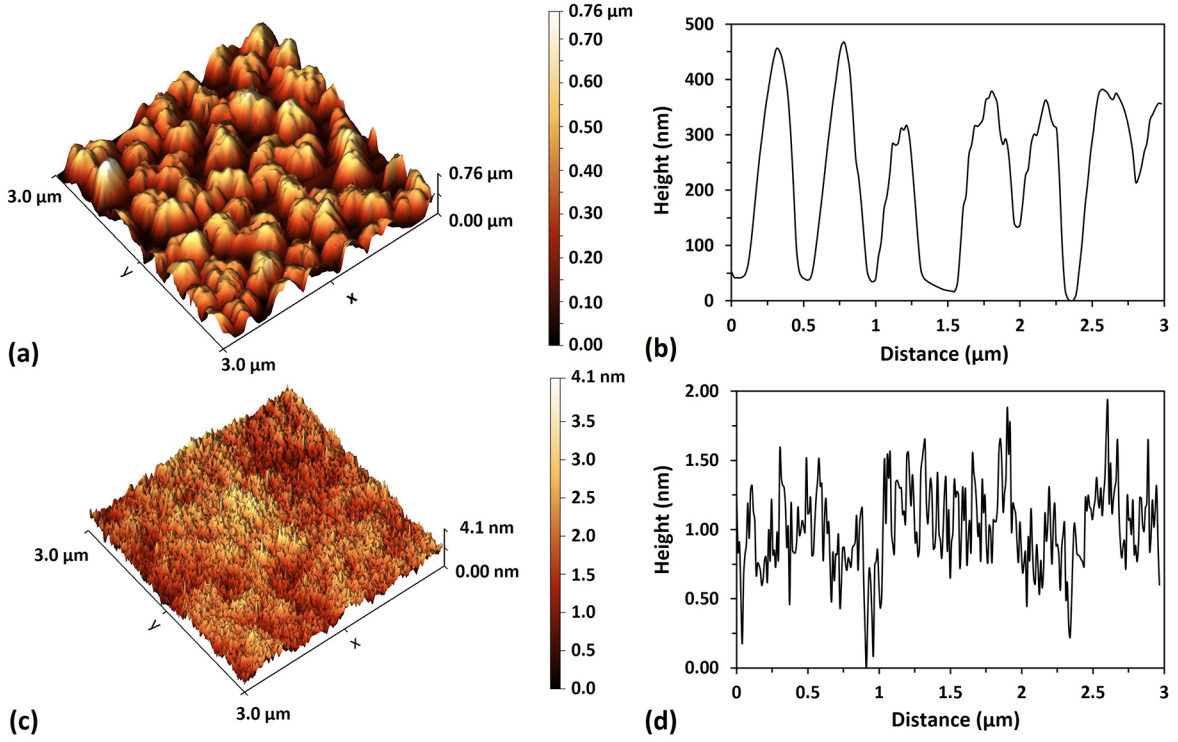

Figure 5. (a) 3D surface plot of plasma-treated PDMS and its (b) height profile; (c) 3D surface plot of pristine PDMS and its (d) height profile.

surface roughness caused by plasma treatment of PDMS (Figures S2–S4 in the Supporting Information show the 3D surface plots of SU8, S1813, and Kapton, respectively). The areal surface roughness parameters S_a, S_q, and S_m were calculated for each material and presented in Table 1. S_a is the arithmetic mean of the peak heights of a surface and is typically used as a measure of surface roughness; S_q is the standard deviation of the peak heights; S_m is the mean

https://doi.org/10.1021/acs.langmuir.1c00689
Langmuir 2021, 37, 8139–8147

Table 1. Areal Surface Roughness Parameters Obtained from AFM Software

process	material	S_a (nm)	S_q (nm)	S_m (nm)	r_{AFM}	S_a:S_m
pristine	PDMS	0.353	0.443	175.0	1.001	0.002
	SU8	0.190	0.238	115.4	1.000	0.002
	S1813	0.222	0.277	135.3	1.000	0.002
	KAPTON	0.639	0.809	99.7	1.002	0.006
plasma treated	PDMS	136.900	156.900	542.5	2.948	0.252
	SU8	32.220	39.750	385.1	1.390	0.084
	S1813	43.380	54.640	425.9	1.336	0.102
	KAPTON	39.990	50.560	390.6	1.373	0.102

separation between peaks; r_{AFM} is the ratio of the total surface area of a rough surface to its projected surface area, which corresponds to an estimate of the Wenzel fraction.

Comparisons of these values can give insight into how much the contact area is reduced. Comparing S_a and S_q show that there is at least an order of magnitude increase in surface roughness in a plasma-treated material compared to a pristine material. S_m values of plasma-treated materials are roughly 3 times greater than that of pristine materials. Finally, comparisons of height:width aspect ratios of empty regions, estimated by S_a:S_m, of plasma-treated surfaces are roughly 2 orders of magnitude greater than pristine surfaces. These comparisons collectively indicate that a significant amount of material contact area has been replaced with air and strongly indicates that liquid metal droplets on plasma-treated materials are in the Cassie−Baxter state, and that this drop in material contact area is likely a significant contributing factor to the nonwetting property created to the plasma-treatment process.

Estimating Apparent Surface Free Energy. For rough surfaces, one typically calculates the apparent surface free energy to understand its wetting behavior.[58−61] Calculation of apparent surface free energy is typically done using the two probe liquid method developed by Girifalco and Good[62,63] for two liquid systems, and was later used by Fowkes[64,65] to determine the surface free energy of a variety of surfaces. The method uses a polar and nonpolar liquid to determine the surface free energy using the following equation[66]

$$\frac{1}{2}\gamma_{LV}(1+\cos\theta) = \sqrt{\gamma_{SV}^{d}\gamma_{LV}^{d}} + \sqrt{\gamma_{SV}^{p}\gamma_{LV}^{p}} \quad (1)$$

where γ_{LV} is the surface tension of the liquid and θ is the contact angle. γ_{LV}^{d} and γ_{LV}^{p} are the dispersive and polar components, respectively, of the liquid's surface tension. γ_{SV}^{d} and γ_{SV}^{p} are the dispersive and polar components, respectively, of the solid's surface free energy. Note that the sum of the dispersive and polar components will give the total surface free energy.

Two standard liquids with well-known dispersive and polar components are used: deionized water and diiodomethane. The dispersive and polar components of deionized water (DIW) are 21.8 and 51.0 mN/m, respectively, for a total surface tension of 72.8 mN/m.[67] The dispersive and polar components of diiodomethane (DIO) are 50.8 and 0 mN/m, respectively, for a total surface tension of 50.8 mN/m.

Table 2 provides the calculated values for the apparent surface free energy for each surface. The value for pristine PDMS shows a dispersive and polar component that closely matches the value reported in the literature by Owen and Wendt[68] ($\gamma_{SV,PDMS}^{d}$ = 21.7 mN/m and $\gamma_{SV,PDMS}^{p}$ = 1.1 mN/m). After plasma treatment, the dispersive component of the apparent surface free energy reduces and the polar component

Table 2. Apparent Surface Free Energy of Pristine and Plasma-Treated Polymeric Surfaces

process	material	dispersive component (mN/m)	polar component (mN/m)	apparent surface free energy (mN/m)
pristine	PDMS	25.65 ± 0.38	1.61 ± 0.32	27.26 ± 0.71
	SU8	49.11 ± 0.25	0.07 ± 1.71	49.17 ± 1.96
	S1813	37.54 ± 0.50	1.17 ± 1.60	38.71 ± 2.10
	KAPTON	34.16 ± 0.49	0.07 ± 1.11	34.23 ± 1.60
plasma treated	PDMS	20.93 ± 0.27	4.78 ± 1.36	25.71 ± 1.63
	SU8	6.73 ± 0.26	2.43 ± 0.39	9.15 ± 0.65
	S1813	7.04 ± 0.25	1.57 ± 0.36	8.61 ± 0.60
	KAPTON	20.72 ± 0.27	0.00 ± 0.60	20.72 ± 0.87

increases, resulting in a negligible change in the total surface energy. The nonwetting property of plasma-treated PDMS is likely due to the lowering of dispersive forces. Fowkes[64] distinguishes between dispersive forces (purely attractive) from polar forces and metallic bond forces, which can be both attractive and repulsive. A reduction in the purely attractive dispersive forces may be sufficient to prevent the wetting of the liquid metal. This is supported by the drastic reduction in the dispersive forces in the other three plasma-treated materials while the polar forces remain relatively low.

Generalizing the Process to Other Polymers. When considering the results that the same plasma treatment is able to convert four different classes of polymers from wetting to nonwetting surfaces, one seeks a common feature responsible for similar results. One common feature among the four polymers due to the plasma treatment is the surface roughness, which reduces the contact area with the liquid. As previously suggested, the high surface tension of the liquid metal on such a rough surface would naturally create a Cassie−Baxter interface. This suggests that the CF_4/O_2 plasma treatment causes a physical change and can be treated as a general method to convert any polymer surface into a nonwetting surface for gallium-based liquid metals by creating a sub-micron rough surface, allowing a larger number of materials as potential substrates for nonwetting liquid metal applications.

CONCLUSIONS

A brief literature survey indicated that the wetting nature of the oxide skin of gallium-based liquid metals limits the development of liquid metal droplet microfluidics. A simple CF_4/O_2 plasma treatment for 120 s was shown to convert previously wetting polymers to the nonwetting surface for surface-oxidized gallium-based liquid metal droplets. Static contact angle measurements for all plasma-treated polymer surfaces were above 150°. Dynamic contact angle measurements showed that the plasma-treated surface yielded low contact angle hysteresis. XPS analyses indicated that the surface

https://doi.org/10.1021/acs.langmuir.1c00689
Langmuir 2021, 37, 8139−8147

undergoes partial fluorination of methyl groups, helping to lower the surface energy. AFM analyses showed an order of magnitude increase in surface roughness, creating a Cassie–Baxter state for the high surface tension liquid metal. Apparent surface free energy calculations show an overall reduction in dispersive forces indicating that the reduction in effective surface area due to Cassie–Baxter state is the cause of nonwetting. Since this plasma treatment created nonwetting surfaces from wetting through a physical change of the surface, it is reasonable that this plasma treatment may be generally used to convert other wetting organic polymers to nonwetting surfaces, which would be useful to explore new liquid metal applications that require nonwetting surfaces.

■ ASSOCIATED CONTENT

Supporting Information

The Supporting Information is available free of charge at https://pubs.acs.org/doi/10.1021/acs.langmuir.1c00689.

XPS survey plots of S1813 and Kapton (Figure S1); 3D surface plots of surface roughness of SU8-2010 (Figure S2); 3D surface plots of surface roughness of S1813 (Figure S3); and 3D surface plots of surface roughness of Kapton tape (Figure S4) (PDF)

■ AUTHOR INFORMATION

Corresponding Author

Jeong-Bong Lee − *Department of Electrical and Computer Engineering, University of Texas at Dallas, Richardson, Texas 75080, United States;* orcid.org/0000-0002-4349-9732; Email: jblee@utdallas.edu

Authors

Sachin Babu − *Department of Electrical and Computer Engineering, University of Texas at Dallas, Richardson, Texas 75080, United States;* orcid.org/0000-0001-8827-4417

Behnoush Dousti − *Department of Electrical and Computer Engineering, University of Texas at Dallas, Richardson, Texas 75080, United States;* orcid.org/0000-0002-7475-8178

Gil Sik Lee − *Department of Electrical and Computer Engineering, University of Texas at Dallas, Richardson, Texas 75080, United States*

Complete contact information is available at: https://pubs.acs.org/10.1021/acs.langmuir.1c00689

Notes

The authors declare no competing financial interest.

■ ACKNOWLEDGMENTS

The authors would like to acknowledge Prof. S.M. You and his group for the use of their KRÜSS DSA30B system. The authors also acknowledge Ziyu Chen for technical discussion and the UT Dallas Clean Room staff for their support of this work. This work was supported in part by the United States National Science Foundation grant NSF ECCS-1908779, NSF ECCS-1710824, and NSF ECCS-1307997.

■ REFERENCES

(1) Liu, T.; Sen, P.; Kim, C.-J. Characterization of Nontoxic Liquid-Metal Alloy Galinstan for Applications in Microdevices. *J. Microelectromech. Syst.* **2012**, *21*, 443–450.

(2) Cooper, C. B.; Arutselvan, K.; Liu, Y.; Armstrong, D.; Lin, Y.; Khan, M. R.; Genzer, J.; Dickey, M. D. Stretchable Capacitive Sensors of Torsion, Strain, and Touch Using Double Helix Liquid Metal Fibers. *Adv. Funct. Mater.* **2017**, *27*, No. 1605630.

(3) Shin, G.; Jeon, B.; Park, Y.-L. Direct Printing of Sub-30 Mm Liquid Metal Patterns on Three-Dimensional Surfaces for Stretchable Electronics. *J. Micromech. Microeng.* **2020**, *30*, No. 034001.

(4) Khondoker, M. A. H.; Sameoto, D. Fabrication Methods and Applications of Microstructured Gallium Based Liquid Metal Alloys. *Smart Mater. Struct.* **2016**, *25*, No. 093001.

(5) Dickey, M. D. Stretchable and Soft Electronics Using Liquid Metals. *Adv. Mater.* **2017**, *29*, No. 1606425.

(6) Mohammed, M. G.; Kramer, R. All-Printed Flexible and Stretchable Electronics. *Adv. Mater.* **2017**, *29*, No. 1604965.

(7) Cheng, S.; Rydberg, A.; Hjort, K.; Wu, Z. Liquid Metal Stretchable Unbalanced Loop Antenna. *Appl. Phys. Lett.* **2009**, *94*, No. 144103.

(8) Hayes, G. J.; So, J.-H.; Qusba, A.; Dickey, M. D.; Lazzi, G. Flexible Liquid Metal Alloy (EGaIn) Microstrip Patch Antenna. *IEEE Trans. Antennas Propag.* **2012**, *60*, 2151–2156.

(9) Kim, D.; Pierce, R. G.; Henderson, R.; Doo, S. J.; Yoo, K.; Lee, J.-B. Liquid Metal Actuation-Based Reversible Frequency Tunable Monopole Antenna. *Appl. Phys. Lett.* **2014**, *105*, No. 234104.

(10) Rashed Khan, M.; Hayes, G. J.; So, J.-H.; Lazzi, G.; Dickey, M. D. A Frequency Shifting Liquid Metal Antenna with Pressure Responsiveness. *Appl. Phys. Lett.* **2011**, *99*, No. 013501.

(11) Yao, B.; Xu, X.; Zhang, Q.; Yu, H.; Li, H.; Ren, L.; Perini, S.; Lanagan, M.; Wang, Q.; Wang, H. Highly Stretchable and Mechanically Tunable Antennas Based on Three-Dimensional Liquid Metal Network. *Mater. Lett.* **2020**, *270*, No. 127727.

(12) Chen, C.H.; Peroulis, D. In *Liquid Metal Droplets for RF MEMS Switches*, Digest of Papers. 2006 Topical Meeting on Silicon Monolithic Integrated Circuits in RF Systems; IEEE, 2006; p 4.

(13) Shen, W.; Edwards, R. T.; Kim, C. J. Electrostatically Actuated Metal-Droplet Microswitches Integrated on CMOS Chip. *J. Microelectromech. Syst.* **2006**, *15*, 879–889.

(14) Chen, C.-H.; Peroulis, D. Liquid RF MEMS Wideband Reflective and Absorptive Switches. *IEEE Trans. Microwave Theory Tech.* **2007**, *55*, 2919–2929.

(15) Sen, P.; Kim, C.-J. C. Microscale Liquid-Metal Switches—A Review. *IEEE Trans. Ind. Electron.* **2009**, *56*, 1314–1330.

(16) Bilodeau, R. A.; Zemlyanov, D. Y.; Kramer, R. K. Liquid Metal Switches for Environmentally Responsive Electronics. *Adv. Mater. Interfaces* **2017**, *4*, No. 1600913.

(17) Wang, Z.; Wang, X.; Miao, Q.; Zhao, Y.-P. Realization of Self-Rotating Droplets Based on Liquid Metal. *Adv. Mater. Interfaces* **2021**, *8*, No. 2001756.

(18) Wang, Z.; Wang, X.; Miao, Q.; Gao, F.; Zhao, Y.-P. Spontaneous Motion and Rotation of Acid Droplets on the Surface of a Liquid Metal. *Langmuir* **2021**, *37*, 4370–4379.

(19) Li, M.; Yu, B.; Behdad, N. Liquid-Tunable Frequency Selective Surfaces. *IEEE Microwave Wireless Compon. Lett.* **2010**, *20*, 423–425.

(20) Li, M.; Behdad, N. Fluidically Tunable Frequency Selective/Phase Shifting Surfaces for High-Power Microwave Applications. *IEEE Trans. Antennas Propag.* **2012**, *60*, 2748–2759.

(21) Gurrala, P.; Oren, S.; Liu, P.; Song, J.; Dong, L. Fully Conformal Square-Patch Frequency-Selective Surface Toward Wearable Electromagnetic Shielding. *IEEE Antennas Wireless Propag. Lett.* **2017**, *16*, 2602–2605.

(22) Ghosh, S.; Lim, S. A Multifunctional Reconfigurable Frequency-Selective Surface Using Liquid-Metal Alloy. *IEEE Trans. Antennas Propag.* **2018**, *66*, 4953–4957.

(23) Ladd, C.; So, J.-H.; Muth, J.; Dickey, M. D. 3D Printing of Free Standing Liquid Metal Microstructures. *Adv. Mater.* **2013**, *25*, 5081–5085.

(24) Tang, S.-Y.; Zhu, J.; Sivan, V.; Gol, B.; Soffe, R.; Zhang, W.; Mitchell, A.; Khoshmanesh, K. Creation of Liquid Metal 3D Microstructures Using Dielectrophoresis. *Adv. Funct. Mater.* **2015**, *25*, 4445–4452.

(25) Parekh, D. P.; Ladd, C.; Panich, L.; Moussa, K.; Dickey, M. D. 3D Printing of Liquid Metals as Fugitive Inks for Fabrication of 3D Microfluidic Channels. *Lab Chip* **2016**, *16*, 1812−1820.
(26) Yu, Y.; Liu, F.; Zhang, R.; Liu, J. Suspension 3D Printing of Liquid Metal into Self-Healing Hydrogel. *Adv. Mater. Technol.* **2017**, *2*, No. 1700173.
(27) Yu, Y.-Z.; Lu, J.-R.; Liu, J. 3D Printing for Functional Electronics by Injection and Package of Liquid Metals into Channels of Mechanical Structures. *Mater. Des.* **2017**, *122*, 80−89.
(28) Kim, D.; Yoo, J. H.; Lee, Y.; Choi, W.; Yoo, K.; Lee, J.-B. In *Gallium-Based Liquid Metal Inkjet Printing*, 2014 IEEE 27th International Conference on Micro Electro Mechanical Systems (MEMS); IEEE, 2014; pp 967−970.
(29) Fassler, A.; Majidi, C. Liquid-Phase Metal Inclusions for a Conductive Polymer Composite. *Adv. Mater.* **2015**, *27*, 1928−1932.
(30) Kazem, N.; Hellebrekers, T.; Majidi, C. Soft Multifunctional Composites and Emulsions with Liquid Metals. *Adv. Mater.* **2017**, *29*, No. 1605985.
(31) Markvicka, E. J.; Bartlett, M. D.; Huang, X.; Majidi, C. An Autonomously Electrically Self-Healing Liquid Metal−Elastomer Composite for Robust Soft-Matter Robotics and Electronics. *Nat. Mater.* **2018**, *17*, 618−624.
(32) Doudrick, K.; Liu, S.; Mutunga, E. M.; Klein, K. L.; Damle, V.; Varanasi, K. K.; Rykaczewski, K. Different Shades of Oxide: From Nanoscale Wetting Mechanisms to Contact Printing of Gallium-Based Liquid Metals. *Langmuir* **2014**, *30*, 6867−6877.
(33) Scharmann, F.; Cherkashinin, G.; Breternitz, V.; Knedlik, C.; Hartung, G.; Weber, T.; Schaefer, J. A. Viscosity Effect on GaInSn Studied by XPS. *Surf. Interface Anal.* **2004**, *36*, 981−985.
(34) Tadmor, R.; Das, R.; Gulec, S.; Liu, J.; E N'guessan, H.; Shah, M.; S Wasnik, P.; Yadav, S. B. Solid−Liquid Work of Adhesion. *Langmuir* **2017**, *33*, 3594−3600.
(35) Garrad, M.; Chen, H.-Y.; Conn, A. T.; Hauser, H.; Rossiter, J. Liquid Metal Logic for Soft Robotics. *IEEE Rob. Autom. Lett.* **2021**, *6*, 4095−4102.
(36) Tang, W.; Jiang, T.; Fan, F. R.; Yu, A. F.; Zhang, C.; Cao, X.; Wang, Z. L. Liquid-Metal Electrode for High-Performance Triboelectric Nanogenerator at an Instantaneous Energy Conversion Efficiency of 70.6%. *Adv. Funct. Mater.* **2015**, *25*, 3718−3725.
(37) Li, G.; Parmar, M.; Kim, D.; Lee, J.-B.; Lee, D.-W. PDMS Based Coplanar Microfluidic Channels for the Surface Reduction of Oxidized Galinstan. *Lab Chip* **2014**, *14*, 200−209.
(38) Kim, D.; Thissen, P.; Viner, G.; Lee, D.-W.; Choi, W.; Chabal, Y. J.; Lee, J.-B. Recovery of Nonwetting Characteristics by Surface Modification of Gallium-Based Liquid Metal Droplets Using Hydrochloric Acid Vapor. *ACS Appl. Mater. Interfaces* **2013**, *5*, 179−185.
(39) Gough, R. C.; Dang, J. H.; Morishita, A. M.; Ohta, A. T.; Shiroma, W. A. In *Frequency-Tunable Slot Antenna Using Continuous Electrowetting of Liquid Metal*, 2014 IEEE MTT-S International Microwave Symposium (IMS2014); IEEE, 2014; pp 1−4.
(40) Wang, M.; Trlica, C.; Khan, M. R.; Dickey, M. D.; Adams, J. J. A Reconfigurable Liquid Metal Antenna Driven by Electrochemically Controlled Capillarity. *J. Appl. Phys.* **2015**, *117*, No. 194901.
(41) Varga, M.; Ladd, C.; Ma, S.; Holbery, J.; Tröster, G. On-Skin Liquid Metal Inertial Sensor. *Lab Chip* **2017**, *17*, 3272−3278.
(42) Chen, Z.; Lee, J. B. Surface Modification with Gallium Coating as Nonwetting Surfaces for Gallium-Based Liquid Metal Droplet Manipulation. *ACS Appl. Mater. Interfaces* **2019**, *11*, 35488−35495.
(43) Ma, J.; Bharambe, V. T.; Persson, K. A.; Bachmann, A. L.; Joshipura, I. D.; Kim, J.; Oh, K. H.; Patrick, J. F.; Adams, J. J.; Dickey, M. D. Metallophobic Coatings to Enable Shape Reconfigurable Liquid Metal Inside 3D Printed Plastics. *ACS Appl. Mater. Interfaces* **2021**, *13* (11), 12709−12718.
(44) Kim, D. *Microfluidic Platforms for Gallium-Based Liquid Metal Alloy*; University of Texas at Dallas, 2014.
(45) Kim, D.; Lee, D.-W.; Choi, W.; Lee, J.-B. A Super-Lyophobic 3-D PDMS Channel as a Novel Microfluidic Platform to Manipulate Oxidized Galinstan. *J. Microelectromech. Syst.* **2013**, *22*, 1267−1275.
(46) Yoo, J. H. A Study on Polymeric Microfluidic and Implantable Neural Devices. Ph.D.Thesis, The University of Texas at Dallas: Texas, United States, 2016.
(47) Li, G.; Parmar, M.; Lee, D.-W. An Oxidized Liquid Metal-Based Microfluidic Platform for Tunable Electronic Device Applications. *Lab Chip* **2015**, *15*, 766−775.
(48) Makkonen, L. A Thermodynamic Model of Contact Angle Hysteresis. *J. Chem. Phys.* **2017**, *147*, No. 064703.
(49) Xiu, Y.; Zhu, L.; Hess, D. W.; Wong, C. P. Relationship between Work of Adhesion and Contact Angle Hysteresis on Superhydrophobic Surfaces. *J. Phys. Chem. C* **2008**, *112*, 11403−11407.
(50) Tadmor, R.; Bahadur, P.; Leh, A.; N'guessan, H. E.; Jaini, R.; Dang, L. Measurement of Lateral Adhesion Forces at the Interface between a Liquid Drop and a Substrate. *Phys. Rev. Lett.* **2009**, *103*, No. 266101.
(51) Boreyko, J. B.; Chen, C.-H. Restoring Superhydrophobicity of Lotus Leaves with Vibration-Induced Dewetting. *Phys. Rev. Lett.* **2009**, *103*, No. 174502.
(52) Manca, M.; Cortese, B.; Viola, I.; Aricò, A. S.; Cingolani, R.; Gigli, G. Influence of Chemistry and Topology Effects on Superhydrophobic CF4-Plasma-Treated Poly(Dimethylsiloxane) (PDMS). *Langmuir* **2008**, *24*, 1833−1843.
(53) Wang, Y.; Bachman, M.; Sims, C. E.; Li, G. P.; Allbritton, N. L. Simple Photografting Method to Chemically Modify and Micropattern the Surface of SU-8 Photoresist. *Langmuir* **2006**, *22*, 2719−2725.
(54) Seethapathy, S.; Górecki, T. Applications of Polydimethylsiloxane in Analytical Chemistry: A Review. *Anal. Chim. Acta* **2012**, *750*, 48−62.
(55) del Campo, A.; Greiner, C. SU-8: A Photoresist for High-Aspect-Ratio and 3D Submicron Lithography. *J. Micromech. Microeng.* **2007**, *17*, R81−R95.
(56) Bratt, A.; Barron, A. XPS of Carbon Nanomaterials. Carbon Nanotubes—OpenStax CNX. https://cnx.org/contents/oDCdCjdZ@1.1:_d2_mDnO/XPS-of-Carbon-Nanomaterials (accessed Sept 12, 2020).
(57) Cordeiro, A. L.; Nitschke, M.; Janke, A.; Helbig, R.; D'Souza, F.; Donnelly, G. T.; Willemsen, P. R.; Werner, C. Fluorination of poly (dimethylsiloxane) surfaces by low pressure CF4 plasma−physicochemical and antifouling properties. *Express Polym. Lett.* **2009**, *3*, 70−83.
(58) Mahadik, D. B.; Venkateswara Rao, A.; Parale, V. G.; Kavale, M. S.; Wagh, P. B.; Ingale, S. V.; Gupta, S. C. Effect of Surface Composition and Roughness on the Apparent Surface Free Energy of Silica Aerogel Materials. *Appl. Phys. Lett.* **2011**, *99*, No. 104104.
(59) Barshilia, H. C.; Mohan, D. K.; Selvakumar, N.; Rajam, K. S. Effect of Substrate Roughness on the Apparent Surface Free Energy of Sputter Deposited Superhydrophobic Polytetrafluoroethylene Thin Films. *Appl. Phys. Lett.* **2009**, *95*, No. 033116.
(60) Chibowski, E. Apparent Surface Free Energy of Superhydrophobic Surfaces. *J. Adhes. Sci. Technol.* **2011**, *25*, 1323−1336.
(61) Yan, Y.; Chibowski, E.; Szcześ, A. Surface Properties of Ti-6Al-4V Alloy Part I: Surface Roughness and Apparent Surface Free Energy. *Mater. Sci. Eng., C* **2017**, *70*, 207−215.
(62) Girifalco, L. A.; Good, R. J. A Theory for the Estimation of Surface and Interfacial Energies. I. Derivation and Application to Interfacial Tension. *J. Phys. Chem. A* **1957**, *61*, 904−909.
(63) Good, R. J.; Girifalco, L. A. A theory for estimation of surface and interfacial energies. III. Estimation of surface energies of solids from contact angle data. *J. Phys. Chem. A* **1960**, *64*, 561−565.
(64) Fowkes, F. M. Attractive Forces at Interfaces. *Ind. Eng. Chem.* **1964**, *56*, 40−52.
(65) Fowkes, F. M. Characterization of Solid Surfaces by Wet Chemical Techniques. In *Industrial Applications of Surface Analysis*; ACS Symposium Series, 1982; Vol. *199*, pp 69−88.
(66) Law, K.-Y.; Zhao, H. *Surface Wetting: Characterization, Contact Angle, and Fundamentals*; Springer: Switzerland, 2016.

https://doi.org/10.1021/acs.langmuir.1c00689
Langmuir 2021, 37, 8139−8147

(67) van Oss, C. J.; Good, R. J.; Busscher, R. J. Estimation of the Polar Surface Tension Parameters of Glycerol and Formamide, for Use in Contact Angle Measurements on Polar Solids. *J. Dispersion Sci. Technol.* **1990**, *11*, 75−81.
(68) Owens, D. K.; Wendt, R. C. Estimation of the Surface Free Energy of Polymers. *J. Appl. Polym. Sci.* **1969**, *13*, 1741−1747.

https://doi.org/10.1021/acs.langmuir.1c00689
Langmuir 2021, 37, 8139−8147